Excess entropy scaling law: A potential energy landscape view

Anthony Saliou [1], Philippe Jarry [2], and Noel Jakse [1]
[1] *Université Grenoble Alpes, CNRS, Grenoble INP, SIMaP, F-38000 Grenoble, France*
[2] *C-TEC, Parc Economique Centr'alp, 725 rue Aristide Bergès, CS10027, Voreppe 38341 cedex, France*

(Received 27 May 2021; accepted 28 September 2021; published 21 October 2021)

The relationship between excess entropy and diffusion is revisited by means of large-scale computer simulation combined to supervised learning approach to determine the excess entropy for the Lennard-Jones potential. Results reveal a strong correlation with the properties of the potential energy landscape (PEL). In particular the exponential law holding in the liquid is seen to be linked with the landscape-influenced regime of the PEL whereas the fluidlike power-law corresponds to the free diffusion regime.

DOI: 10.1103/PhysRevE.104.044128

I. INTRODUCTION

Understanding the link between dynamic properties of fluids and their underlying structure and thermodynamics [1–3] remains one of the major open issues in condensed matter physics. The excess entropy scaling law proposed by Rosenfeld [4,5] provides such a link between diffusion, viscosity, as well as thermal diffusion and entropy. It applies for a wide range of systems and thermodynamic states (see Ref. [6]), and, for instance, for pure metals and alloys [7] yielding a simple link between partial entropies and corresponding diffusions of the constitutive elements [8]. It counts, however, a number of counterexamples [6] showing that it remains more a semiquantitative approach. Nevertheless, it was shown to be more general than expected initially in the framework of isomorph theory with hidden scale invariance [6,9–11].

The nonuniversal character of excess entropy law lies on the fact that entropy is basically a macroscopic equilibrium thermodynamic quantity whereas diffusion emerges from the rate of transition between underlying accessible microscopic states [6]. A unified picture that may conciliate both these aspects is provided by the potential-energy landscape (PEL) concept [12,13] in which the thermodynamics comes from the relative depths of the PEL minima whereas the dynamics is guided by their connectivity [14]. The effect of complexity of the PEL on Rosenfeld's exponential law was investigated through a Gaussian random interacting potential and showed that it still holds for moderate disorder [15]. A linear relationship between local characteristics of the PEL and diffusivity assuming the excess entropy scaling was shown [16]. Nevertheless, a more general link between the PEL and the excess scaling law is still missing to date.

The aim of the present paper is to provide a deeper insight on the excess entropy scaling law through the PEL concepts highlighted here for the Lennard-Jones (LJ) potential. The choice of the LJ model was guided by the fact that it leads to a quasiuniversal character of the excess entropy scaling [5]. This led us first to determine accurately the entropy over the largest fluid domain of the $\rho^* - T^*$ phase diagram, where $\rho^* = \rho\sigma^3$ and $T^* = k_B T/\epsilon$ and σ being the LJ length and energy scales, respectively. This nontrivial task [17] is achieved by setting up a supervised machine learning (ML) approach using artificial neural networks (ANNs) [18,19]. It allows us to combine databases covering different thermodynamic domains irrespective of the mathematical formulation of their equation of states (EOS) without loss off accuracy. It was proven recently to be efficient to investigate the crystal nucleation by Monte Carlo simulation taking entropy as a reaction coordinate [20]. The second part consists in conducting large-scale molecular dynamics (MD) simulations [21] to generate an accurate, consistent, and homogeneous dataset of self-diffusion coefficients spanning over the same range of the fluid phase diagram. Our findings show that the general characteristics of the PEL might be linked to the excess entropy scaling, i.e., Rosenfeld's exponential law is seen to be correlated with the landscape influenced part of the PEL [13] whereas the fluidike power law corresponds to its free diffusion regime.

The layout of the paper is the following. Section II is devoted to the method by which the entropy is determined, and Sec. III presents the results that reveal the correlation between the excess entropy law crossover and the potential energy landscape. Finally, Sec. IV provides the main conclusion of the paper.

II. DETERMINATION OF THE EXCESS ENTROPY

A. Constructing the dataset

The entropy is determined in two steps from the basic thermodynamic relation $S_{ex} = (U_{ex} - A_{ex})/T$, where U_{ex} is the excess internal energy and A_{ex} the excess Helmholtz free energy. For the latter, many EOS were proposed in the literature [22,23] that are valid over various domains of the phase diagram. Here, the Johnson *et al.* EOS [24] for temperature domain $0.5 < T^* \leqslant 6.0$ and the one for higher temperatures in the range $6.0 < T^* \leqslant 9.0$ of Thol *et al.* was used. Considering densities from 0.005 to $\rho^* = 1.2$ allows us to cover

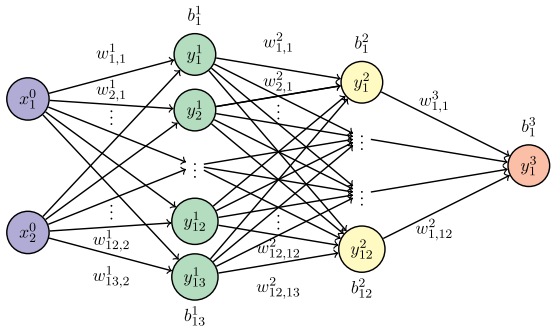

FIG. 1. Schematic of the feedforward neural network built as densely connected multilayer perceptrons. The input layer $\{x_1^0; x_2^0\}$ will be fed with density ρ^* and temperature T^* couples of the training set, and the output y_1^3 takes the value of corresponding excess Helmholtz free energy $A_{\rm ex}^*$. The neural network contains two hidden layers with superscripts 1 and 2, respectively. The first layer is composed of 13 neurons, and the second one is composed of 12. The weights w_{ijk}^l and bias b_i^l are optimized during the training (see the text).

a range of pressures up to $P^* = P\sigma^3\epsilon = 50$. In this domain, using the respective EOS equations the dataset is composed of 16 448 values of $A_{\rm ex}^* = A_{\rm ex}/\epsilon$ for regularly spaced couples (ρ^*, T^*) in the domain defined above. The typical temperature and density meshes are $0.065\epsilon/k_B$ and $0.015\sigma^{-3}$, respectively. The data points in the unstable liquid-gas coexistence region were removed.

The complete dataset is primarily randomized and scaled with

$$\mathrm{SS}(x) = \frac{x - m(x)}{\sigma(x)}, \tag{1}$$

where m refers to the mean and σ refers to the standard deviation, whereas x is an input series of the dataset. The training set consists in taking 80% of the dataset, the remaining part is left for the test set. The training set is further split to get a validation set, which amounts to 20% of the training observations.

B. Supervised learning approach

In a first step, $A_{\rm ex}$ is determined from a supervised learning process using an artificial neural network. The ANN is defined by a network topology which specifies the number of neurons formally named here y_{ij}^l and their connectivity through the weights w_i^l. Figure 1 represents schematically the typical architecture used in the present paper, called a multilayer perceptron. The weights associated with each node pairs are optimized during the learning process by a feedforward technique [25]. Thus, each of the N layers within the neural network consists of sets of nodes which receive multiple inputs from the previous layer and pass outputs to the next layer. Here a fully connected network is used in which every output of a layer is an input for every neuron in the next layer. The corresponding mathematical description is the following: The inputs signals are linearly combined before being activated by function f to give each output y_i^l of a given fully connected layer l as

$$y_i^l = f\left(\sum_{j=1}^{N_{l-1}} w_{ij}^l y_j^{l-1} + b_i^l\right), \tag{2}$$

where N_l refers to the size of the lth layer, i.e., the number of neurons in the layer. Note that positive weights enhance connections whereas negative weights tend to inhibit them. Most of the activation function are choose to have a range in either [0,1] or [−1, 1] and modulates the amplitude of the output. The activation function f is applied elementwise and is taken as the hyperbolic tangent form $f(x) = \tanh(x)$. Backpropagation is used to update the network weights and their the gradients. The ANN was coded using the KERAS module from the TENSORFLOW PYTHON package [26] in the regression mode.

C. Training the artificial neural network

The supervised training is carried out using the macroscopic two-component descriptor $(\rho^*; T^*)$ as the input, and the corresponding $A_{\rm ex}^*$ as the output to find the optimal set of weights and biases. For a given architecture, the optimization is performed using the training data alone, terminating when the validation error begins to increase. Simultaneously, a L_2 norm regularization is performed to check for consistency. An early stopping criterion is used on training and validation sets to avoid overfitting the training data. Once trained, the ANN was used to predict $A_{\rm ex}^*$ whatever the temperature and density inside the above defined domain allowing us to predict the excess entropy with a high accuracy by simply using the internal energy from the corresponding MD simulation.

This training stage is repeated with various ANN architectures to find the optimal one capturing numerically at best the functional dependence of the data. The minimization of the mean-square error (MSE) is carried out with stochastic gradient descent using the Adam optimization algorithm [25] giving a measure of the loss with a constant learning rate of 0.001, $\beta_1 = 0.9$, $\beta_2 = 0.999$, and $\varepsilon = 10^{-8}$. The early stopping was performed with maximum loss variation of 10^{-6} and a patience of 45 epochs. The least MSE loss is obtained for an architecture of 13 and 12 neurons in the first and second hidden layers, respectively, as depicted in Fig. 1. A cross validation performed over ten independent trainings gives a loss of $(2.3 \pm 0.4) \times 10^{-4}\epsilon$ on the per atom excess Helmholtz free energy. The left panel of Fig. 2 displays the predictive ability of the model on the unseen data of the test set. The quality is very high on the whole range of the free energy with a small deviation at the very end of the large values for which there is less data. The right panel of Fig. 2 shows the evolution of the MSE loss as a function of epochs. The typical duration of the training period was about 10 000 to 15 000 epochs.

D. Molecular dynamics simulations

The MD simulations were performed with $N = 10\,768$ LJ particles in the isobaric-isothermal ensemble (N, P, T) within the Nosé-Hoover scheme [21] using the LAMMPS code [27]. The truncated LJ was used with cutoff radius as large as $r_C = 4\sigma$ and standard long-range corrections [21] were applied to pressures and energies. Equations of motions were

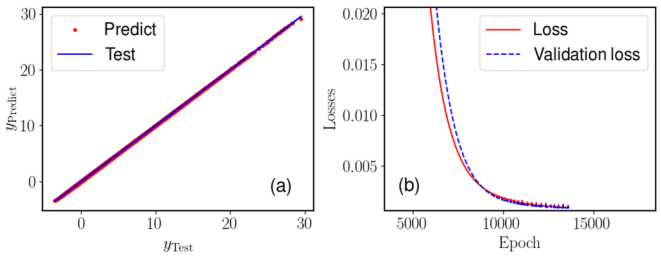

FIG. 2. (a) Train-test curve showing the quality of the prediction on the test set for the optimized NN with 13 and 12 neurons, respectively, in the first and the second hidden layers. The blue solid line represents the known output of the excess Helmholtz free energies, and the red dots represent the values predicted against the known ones. (b) Evolution of the MSE losses as a function of the number of epochs for the training and validation sets.

integrated with velocity-verlet algorithm and a time step $\delta t^* = 0.001$. The chosen large value of N reduces strongly the finite size effects so that corrections on the diffusion coefficients were not necessary [28]. For all the thermodynamic states, the system was equilibrated during 10^5 time steps followed by a production run of 2×10^5 steps during which averaged properties were calculated.

Results along isobar $P^* = 1.0$ are shown in Fig. 3 as a typical example. Those for isobars $P^* = 5.0$ and $P^* = 10.0$, respectively, are shown in Figs. S1 and S2 in the Supplemental Material [29]. Various quantities were collected for all temperatures spaced by temperature step $\Delta T = 0.02$. Below the melting point, the system was cooled down with a fast quenching rate of $Q = 0.01$ to avoid spontaneous crystallization. The dynamical glass transition occurs at the crossover seen on the temperature evolution of the density [panel (b)] and the diffusion [panel (c)]. In panel(a) the excess potential energy with and without long-range corrections are compared, showing that they are always very small. For each generated state point, inherent structure energies [12,13] were determined from a conjugate gradient minimization on five independent configurations. The needed data from these isobars as well as all others were stored in a data set to determine in a post treatment the excess entropy with the machine learning approach.

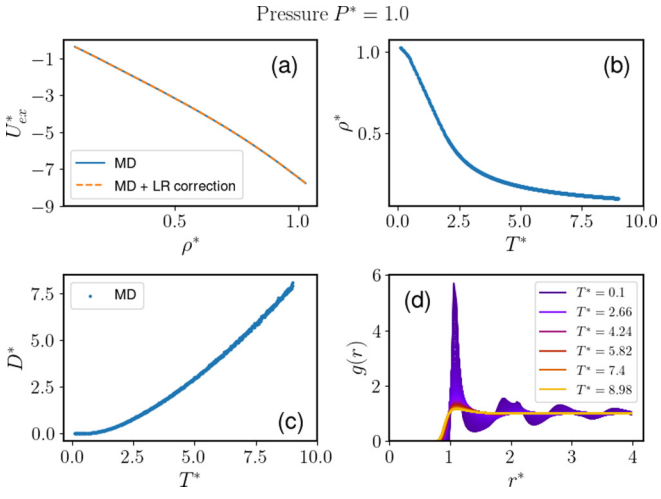

FIG. 3. Molecular dynamics simulation results along isobar $P^* = 1$, namely, excess potential energy (a), density (b), self-diffusion coefficients (c), and pair-correlation functions (d).

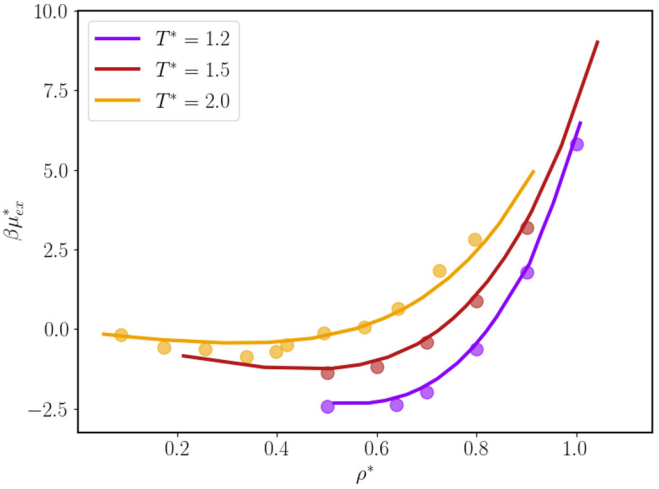

FIG. 4. Excess chemical potential reduced by the temperature ($\beta = 1/T^*$) as a function of density. Predictions of the NN (solid lines) are compared to the direct molecular dynamics simulations (filled circles) of Ref. [30] for isotherms $T^* = 1.5$ and 2 and Ref. [31] for $T^* = 1.2$.

E. Testing the neural network

From the predicted excess Helmholtz free energy $A^*_{\rm ex}$ the excess entropy can be determined readily from MD simulations by the thermodynamic relation,

$$S^*_{\rm ex} = \frac{U^*_{\rm ex} - A^*_{\rm ex}}{T^*}, \tag{3}$$

in which $U^*_{\rm ex}$ is the excess energy. In order to assess the reliability of the approach, results of the excess entropy is compared to independently published MD dynamics simulation [30,31] through the excess chemical potential $\mu_{\rm ex}$ using the standard relation [32],

$$S_{\rm ex} = \frac{\beta P}{\rho} - 1 + \frac{\beta U_{\rm ex}}{\langle N \rangle} - \beta \mu_{\rm ex}, \tag{4}$$

where P is the pressure. Figure 4 shows the excess chemical potential for several isotherms. Good agreement is found for all of them given the fact that the small number of atoms in those simulations tends to underestimate the chemical potential [30].

III. RESULTS AND DISCUSSION

Figure 5 shows the evolution the reduced diffusion by means of Rosenfeld's scaling as a function of $-S^*_{\rm ex} = -S_{\rm ex}/Nk_B$ for all the simulated state points. The latter were obtained along 22 isobars with a temperature step of 0.02 that cover quite homogeneously the considered phase diagram as shown in the inset. In doing so, $-S^*_{\rm ex}$ spans almost over the complete range considered for most of the pressures. Diffusion curves for all isobars collapse nicely onto a master curve for $-S^*_{\rm ex}$ going from 0 in the dilute gas phase to the dense liquid phase even up to roughly 3.9 corresponding to the melting line [34] as will be seen below. Such a behavior

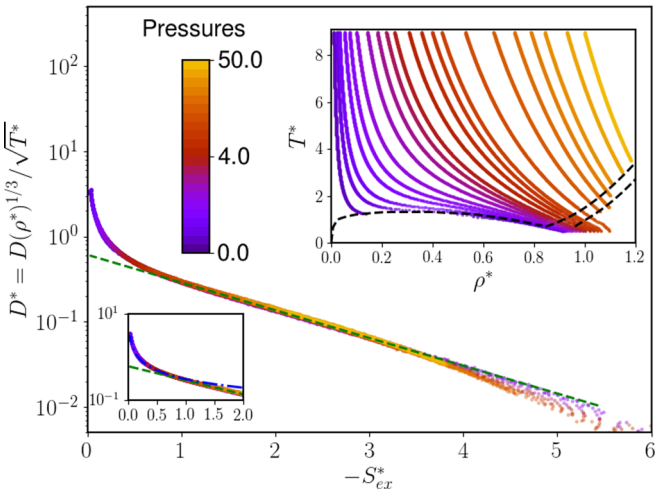

FIG. 5. Scaled diffusion D^* as a function of excess entropy $-S^*_{\rm ex} = -S_{\rm ex}/Nk_B$ along 22 isobars shown in the upper right inset. The green dashed line corresponds to a fit of the diffusion data in the range $1 \leqslant S^*_{\rm ex} \leqslant 3$ with Rosenfeld' law $0.61 * \exp(-0.751 S^*_{\rm ex})$ (see the text). The considered pressures are $P^* =$ 0, 0.1, 0.2, 0.3, 0.5, 0.7, 1, 1.5, 2, 2.5, 3, 4, 5, 6, 7, 10, 15, 20, 25, 30, 40, and 50. The black dashed lines correspond to liquid-gas coexistence after Ref. [33] below $\rho^* = 0.8$ and the solid-liquid coexistence after Ref. [34] above. The lower left inset shows the scaled diffusion in the dilute fluid range with small $-S^*_{\rm ex}$. The blue dashed-dot line corresponds to Rosenfeld's [5] power-law $0.305(-S_{\rm ex})^{-2/3}$.

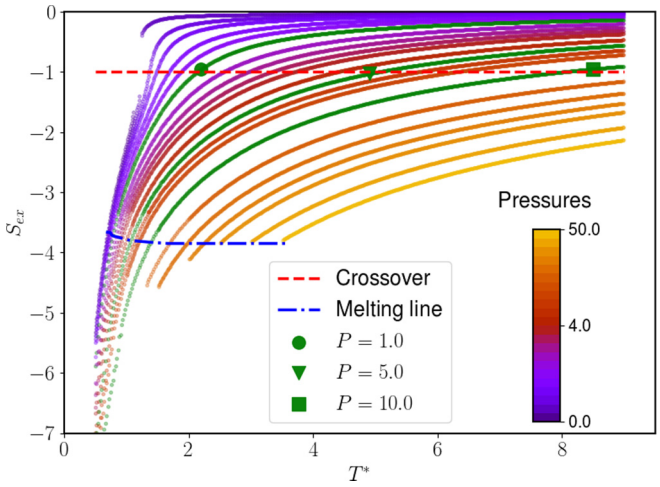

FIG. 6. Excess entropy as a function of temperatures along isobars for all pressures. The blue dashed line corresponds to the melting line inferred from Ref. [34] and the red dashed-dot one marks the crossover at $-S^*_{\rm ex} = 1$ (see the text). The green full circle, triangle, and square represent the onset of free diffusion regime in the potential energy landscape for $P^* = 1.0$, 5.0, and 10.0 as shown in Fig. 7.

is well known and corresponds to Rosenfeld's findings commented several times and nicely reviewed very recently by Dyre [6]. The data shown in the curves have unprecedented low dispersion [22], which can be attributed to the fact that: (i) the diffusion coefficients and corresponding potential energies are extracted from the same body of 17 500 large-scale MD simulations, and (ii) the entropy is obtained consistently using a machine learning approach on accurate EOSs [23,24]. Following Rosenfeld [5], above melting, the excess entropy scaling shows a clear crossover around $-S^*_{\rm ex} \simeq 1$ with a power law for dilute gas below 1, i.e., $0.305(-S_{\rm ex})^{-2/3}$ and the exponential law $0.61 * \exp(-0.751 S^*_{\rm ex})$ above as shown in the lower left inset of Fig. 5. The exponential law was fitted in the range of $0.61 * \exp(-0.751 S^*_{\rm ex})$ including all isobars. It is worth mentioning that with this fitting range, the exponential law still holds even below the melting line for low pressures roughly $P^* \leqslant 0.5$.

Figure 6 displays the temperature evolution of the excess entropy for all considered isobars. The blue dashed line shows the values of $S^*_{\rm ex}$ found for the densities and temperatures corresponding to the melting line taken from Mastny and De Pablo [34]. Interestingly, $S^*_{\rm ex}$ remains quite constant with a value of $\sim$3.85 up to $P^* = 50$ that highlights once more the importance of excess entropy in describing the phases of matter [32]. The dashed red line corresponds to the crossover between the power and the exponential scaling laws as described above. Three green curves were chosen to intersect the crossover over the complete range of temperatures investigated, avoiding them being too close to liquid-gas coexistence line and critical point. They correspond to isobars $P^* = 1.0$, $P^* = 5.0$, and $P^* = 10.0$ that were investigated further by MD to reveal the properties of their underling PEL.

For each temperature above the melting line, an average inherent-structure energy (ISE) [13] over 50 independent configurations was determined by means of conjugate gradient minimization, bringing the system local minimum of the PEL. Below the melting line, the system was first rapidly quenched with a cooling rate of 0.02 before calculating the ISEs in the same manner. The corresponding ISE curves for the three pressures are drawn in Fig. 7 for which an additional Stavitky and Golay smoothing with ten points was applied. A typical behavior as a function of temperature [13] is seen for all the curves with an almost linear regime at high-temperature corresponding to the so-called free diffusion regime that turns to a more pronounced decrease upon further cooling as the system enters the landscape-influenced regime (highlighted by a colored area under the curves). Finally, when the dynamical glass transition is reached, ISE curves remain essentially constant at low temperatures, marking the glassy regime. The turning points between the free diffusion and the landscape influenced regime, marked by symbols were determined by a linear regression by least squares minimization of the free diffusion regime. Decreasing progressively the hypothetical turning point temperature (i.e., increasing the fitting range) the final value was identified when the Pearson correlation coefficient was below a threshold of 0.98. The corresponding p value of the t statistics with a null hypothesis of a nonlinear regression was always below 0.05. The ISEs are seen to decrease with pressure whereas the range of landscape influenced regime widens.

The excess entropy corresponding to the temperature separating the landscape-influenced and the free diffusion regimes determined above for each of the three pressures are also drawn in Fig. 6 with the symbols. An excellent match is found with the crossover in the excess entropy scaling laws,

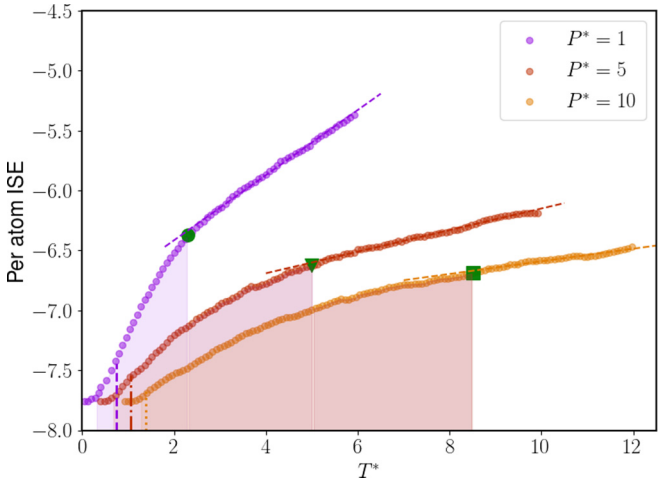

FIG. 7. Inherent structure energy for $P^* = 1.0$, 5.0, and 10.0. The filled areas under the curves correspond to the landscape influenced regime with a lower limit corresponding to the dynamical glass transition of 0.32, 0.67, and 1.20, and a upper limit of 2.32, 5.04, and 8.52, respectively, for $P^* = 1.0$, 5.0, and 10.0. The respective vertical dashed, dashed-dot, and dotted lines mark the melting points, namely, 0.74, 1.06, and 1.379, after Ref. [34]. The green full circle, triangle, and square represent the onset of free diffusion regime in the potential energy landscape.

demonstrating a strong correlation between the two in a wide range of pressures and temperatures. The free diffusion regime is representative of the dilute gas with low density and high-temperature fluid where the PEL is only weakly felt by the system. The latter can be considered as composed of colliding hard sphere particles having a diffusion proportional to the mean free path and thermal velocity. This might be well undertaken in the framework of Enskog's theory [3] from which emerges the power law with exponent 2/3 [5]. For $-S^*_{ex} \geqslant 1$, our results show that Rosenfeld's exponential law might be related to the landscape-influenced regime whatever the pressure. The progressive transition region between weak and strong coupling behaviors of the entropy scaling curve around $-S^*_{ex} \simeq 1$ mirrors the one of the ISE curves between diffusion and landscape-influenced regimes shown in Fig. 7. Although not justified in details by Rosenfeld initially, his macroscopically reduced units involve a general length scale $\rho^{-1/3}$ generally associated with an average distance between particles. It can be interpreted as a mean free path between collisions at low densities that progressively tends to the average interparticle distance as the density increases. Along this line, a modified excess entropy scale was proposed very recently, unifying the two regimes [22].

Although the landscape-influenced regime of the PEL extends to the glass transition by definition [13], the exponential seems to hold generally only above the melting point. Figure 5 indicates, however, that it extends significantly below the melting line for low pressures, consistently with the PEL view. For higher pressure, probably the high density and low pressure thermodynamic states are less well described by the underlying equation of states [24] considered, preventing accurate estimation of the entropy with the ML approach, accuracy known to be crucial [17]. Interestingly, MD simulations with the Kob-Andersen binary LJ model [35] show that excess-entropy scaling still holds down to the mode coupling critical temperature, but the exponential law seems to be limited to moderate undercooling only, recalling though that the configuration entropy was used for the scaling in that case. This prompts us to further investigations below the melting line [36].

IV. CONCLUSION

A significant body of self-diffusion coefficients and potential energies obtained by large-scale molecular dynamics simulation was combined to machine learning to efficiently and accurately determine the entropy for temperatures and pressures ranging to $0.5 < T^* \leqslant 6.0$ and $0 < P^* \leqslant 50.0$, respectively, representative of the essential part of the LJ phase diagram for the fluid phase. Our results reveal that excess-entropy scaling discovered by Rosenfeld is a consequence of the properties of the underlying potential energy landscape. This link reflects the complexity of the PEL. As a matter of facts, local minima of the PEL fix the number of accessible states corresponding to the very definition of the entropy and barrier heights fix the transition rates. Such an intimate relation between the PEL and the dynamics was also demonstrated recently to be quite general for pure liquid metals [37]. Interestingly, as revealed here, the crossover line between the free diffusion and the landscape-influenced regimes as well as the melting line within the pressure range investigated here seem to be excess entropy invariant. For dense liquids, it was shown that isomorph invariance might be the appropriate theoretical framework [6]. Given the link revealed here, it could be more general as the PEL view offers a generalization ground and opens the way for further theoretical developments and understanding.

ACKNOWLEDGMENTS

One of us, N.J., would like to express deep thanks to J. Schwindling for initial discussions and advice on neural networks. We acknowledge the CINES and IDRIS under Project No. INP2227/72914 as well as CIMENT/GRICAD for computational resources. This work was performed within the framework of the Centre of Excellence of Multifunctional Architectured Materials "CEMAM" ANR-10-LABX-44-01 funded by the "Investments for the Future" Program. This work has been partially supported by MIAI@Grenoble Alpes (Grant No. ANR-19-P3IA-0003). Fruitful discussions within the French collaborative network in high-temperature thermodynamics GDR CNRS 3584 (TherMatHT) are also acknowledged.

[1] S. Chapman and T. G. Cowling, *The Mathematical Theory of Non-Uniform Gases* (Cambridge University Press, Cambridge, U.K., 1939).

[2] H. Eyring and J. Hirschfelder, J. Phys. Chem. **41**, 249 (1937).

[3] J.-P. Hansen and I. R. McDonald, *Theory of Simple Liquids*, 3rd ed. (Academic, London, 2006).

[4] Y. Rosenfeld, Phys. Rev. A **15**, 2545 (1977).
[5] Y. Rosenfeld, J. Phys.: Condens. Matter **11**, 5415 (1999).
[6] J. C. Dyre, J. Chem. Phys. **149**, 210901 (2018).
[7] J. J. Hoyt, M. Asta, and B. Sadigh, Phys. Rev. Lett. **85**, 594 (2000).
[8] A. Pasturel and N. Jakse, J. Phys.: Condens. Matter **28**, 485101 (2016).
[9] J. C. Dyre, Phys. Rev. E **88**, 042139 (2013).
[10] J. C. Dyre, J. Phys.: Condens. Matter **28**, 323001 (2016).
[11] T. J. Yoon, M. Y. Ha, E. A. Lazar, W. B. Lee, and Y.-W. Lee, Phys. Rev. E **100**, 012118 (2019).
[12] F. H. Stillinger, Science **267**, 1935 (1995).
[13] S. Sastry, P. G. Debenedetti, and F. H. Stillinger, Nature (London) **393**, 554 (1998).
[14] D. J. Wales, *Energy Landscapes* (Cambridge University Press, Cambridge, U.K., 2003).
[15] K. Seki and B. Bagchi, J. Chem. Phys. **143**, 194110 (2015).
[16] S. N. Chakraborty and C. Chakravarty, J. Chem. Phys. **124**, 014507 (2006).
[17] N. Jakse and A. Pasturel, Sci. Rep. **6**, 20689 (2016).
[18] J. Schmidt, M. R. G. Marques, S. Botti, and M. A. L. Marques, npj Comput. Mater. **5**, 83 (2019).
[19] P. Mehta, M. Bukov, C. H. Wang, A. G. R. Day, C. Richardson, C. K. Fisher, and D. J. Schwab, Phys. Rep. **810**, 1 (2019).
[20] C. Desgranges and J. Delhommelle, Phys. Rev. E **98**, 063307 (2018).
[21] B. Smit and D. Frenkel, *Understanding Molecular Simulations*, 2nd ed. (Academic, San Diego, 2002).
[22] I. H. Bell, R. Messerly, M. Thol, L. Costigliola, and J. C. Dyre, J. Phys. Chem. B **123**, 6345 (2019).
[23] M. Thol, G. Rutkai, A. Köster, R. Lustig, R. Span, and J. Vrabec, J. Phys. Chem. Ref. Data **45**, 023101 (2016).
[24] J. K. Johnson, J. A. Zollweg, and K. E. Gubbins, Mol. Phys. **78**, 591 (1993).
[25] T. Hastie, R. Tibshirani, and J. Friedman, *The Elements of Statistical Learning Data Mining, Inference, and Prediction*, 2nd ed., Springer Series in Statistics (Springer, Berlin, 2008).
[26] The Python package can be found here at https://www.tensorflow.org
[27] S. J. Plimpton, J. Comput. Phys. **117**, 1 (1995).
[28] I.-C. Yeh and G. Hummer, J. Phys. Chem. B **108**, 15873 (2004).
[29] See Supplemental Material at http://link.aps.org/supplemental/10.1103/PhysRevE.104.044128 for additional curves.
[30] R. L. Rowley, T. D. Shupe, and M. W. Schuck, Mol. Phys. **82**, 841 (1994).
[31] L. L. Lee, D. Ghonasgi, and E. Lomba, J. Chem. Phys. **104**, 8058 (1996).
[32] N. Jakse and I. Charpentier, Phys. Rev. E **67**, 061203 (2003).
[33] A. Z. Panagiotopoulos, Int. J. Thermophys. **15**, 1057 (1994).
[34] E. A. Mastny and J. J. De Pablo, J. Chem. Phys. **127**, 104504 (2007).
[35] M. Agarwal, M. Singh, B. S. Jabes, and C. Chakravarty, J. Chem. Phys. **134**, 014502 (2011).
[36] I. H. Bell, J. C. Dyre, and T. S. Ingebrigtsen, Nat. Commun. **11**, 4300 (2020).
[37] F. Demmel, L. Hennet, and N. Jakse, Sci. Rep. **11**, 11815 (2021).